PNAS RESEARCH ARTICLE | CHEMISTRY

Long-lived polaritonic coherence and polaron decoupling effects in 2D electronic spectra

M. Elious Mondal[a], Seongje Park[b,c], Minjung Son[b,c], A. Nickolas Vamivakas[d,e,f], Steven T. Cundiff[g], Todd D. Krauss[a,d,f], and Pengfei Huo[a,d,f,1]

Affiliations are included on p. 9.

Edited by Angel Rubio, Max-Planck-Institut fur Struktur und Dynamik der Materie, Hamburg, Germany; received October 29, 2025; accepted March 18, 2026

Molecular polaritons, formed by coupling molecular excitons with cavity photons, offer a promising platform for exploring quantum phenomena. A key challenge is understanding how these hybrid states maintain coherence in the presence of environmental vibrations. Here, we show theoretically that collective coupling of many molecular excitons in a cavity can protect polariton coherence from phonon-induced decoherence. Under realistic conditions, the coherence time can extend up to 200 fs at room temperature, compared with 15 fs for typical molecular systems. Simulations of two-dimensional electronic spectra reveal prolonged oscillations between upper and lower polariton states, and reduced vibrational coupling as indicated by changes in the nodal line slope of the lower polariton peak. These findings provide guidance for experimental efforts to realize long-lived polaritons, such as coupling CdSe nanoplatelets to optical cavities.

exciton polariton | 2D electronic spectroscopy | coherence enhancement | polaron decoupling

Significance

Optical cavity polaritons are novel quantum systems that promise significant advancement in quantum information science. The cavity photon hybridizes with the collective exciton of molecules through collective light–matter couplings and effectively reduces the coupling with the vibrations, known as the polaron decoupling effect. Nonlinear spectroscopy is the ideal tool to provide information on both coherence time and vibronic couplings. This work provides strong theoretical evidence that the collective light–matter coupling leads to long-lived polariton coherence in the nonlinear 2D electronic spectra. It theoretically demonstrates the prolonged polariton coherence as the beating between the UP and LP polariton states, as well as the polaron decoupling effect through nodal line slope reductions.

Coupling molecules to a quantized radiation field inside an optical cavity produces a set of photon-matter hybrid (entangled) states known as polaritons (Fig. 1*A*). These polariton states, which are hybridizations of the excitons and photons, have been shown to possess the properties of both and have enabled novel many-body physics, new chemical reactivities (1), and intriguing spectroscopic signals (2–6). In particular, due to the collective light–matter coupling, the polariton states are effectively decoupled from the molecular vibrations, which is referred to as the polaron decoupling effect (2, 7, 8). The polaron decoupling effect has been experimentally verified by linear spectra (3, 4, 9), as well as nonlinear two-dimensional electronic Spectroscopy (2DES) (2). Due to the effective polaron decoupling effect, it is possible to achieve a long-lived polaritonic coherence even at room temperature. Indeed, our preliminary theoretical work(10) suggests that it is possible to prolong the exciton coherence from the original 15 fs to exciton–polariton coherence up to 200 fs in a model system with parameters that describes CdSe Nanoplatelets (NPL) coupled to an optical cavity (11–14), with the explicit consideration of both cavity loss and decay to the dark states (10, 15). Nonlinear polariton 2DES (2, 5, 16–19) is the ideal technique to provide information on polariton coherence (Fig. 1*B*). Experimentally, the off-diagonal beating signal (Fig. 1*C*) has not been clearly observed, likely due to the low quality factor of the plasmonic cavity (16) as well as large disorders in the organic molecules (16–18) that couple to the cavity. Theoretically, there are several exciting developments in simulating 2DES of molecular polaritons (20–23). However, a direct theoretical verification of such prolonged coherence in 2DES remains missing due to both the computational challenge to accurately simulate 2DES spectra while taking care of the non-Markovian behavior of the phonon dynamics, and explicitly considering the cavity loss. To address this missing link, we propose to couple CdSe NPL (11) to a high-quality Fabry–Perot (FP) cavity (13) as an experimental platform, and theoretically investigate the possibility of observing long-lived polariton coherence under room temperature. The CdSe NPL exhibits nearly zero inhomogeneous broadening (11, 13), such that the linear spectra linewidths are nearly identical for the single NC and for the ensemble (11). Theoretically, we use state-of-the-art theoretical approaches (15, 24, 25) we have developed to accurately and efficiently simulate polariton 2DES spectra, allowing us to reveal prolonged off-diagonal beating between the upper and lower polariton states (Fig. 1*C*), which aligns with polaron decoupling effects also indicated by the flattening of nodal line slope (NLS) of diagonal peaks in pure-absorptive 2DES (Fig. 1*D*).

Author contributions: M.E.M., S.P., M.S., A.N.V., S.T.C., T.D.K., and P.H. designed research; M.E.M. and P.H. performed research; M.E.M., M.S., S.T.C., T.D.K., and P.H. contributed new reagents/analytic tools; M.E.M., S.P., M.S., A.N.V., S.T.C., T.D.K., and P.H. analyzed data; and M.E.M., S.P., M.S., A.N.V., S.T.C., T.D.K., and P.H. wrote the paper.

The authors declare no competing interest.

This article is a PNAS Direct Submission.

[1]To whom correspondence may be addressed. Email: pengfei.huo@rochester.edu.

This article contains supporting information online at https://www.pnas.org/lookup/suppl/doi:10.1073/pnas.2530454123/-/DCSupplemental.

Published April 21, 2026.

Theoretical Model

We use the Holstein–Tavis–Cummings (HTC) Hamiltonian (11, 24, 26) to describe N-molecules collectively coupled to a single cavity mode as follows

$$\hat{H} = \sum_{n=1}^{N} \varepsilon_n \hat{\sigma}_n^\dagger \hat{\sigma}_n + \hat{H}_{\mathrm{sb}} + \hat{H}_{\mathrm{b}} + \hbar\omega_{\mathrm{c}}\left(\hat{a}^\dagger \hat{a} + \frac{1}{2}\right) + \sum_{n=1}^{N} \hbar g_{\mathrm{c}} \left(\hat{\sigma}_n^\dagger \hat{a} + \hat{\sigma}_n \hat{a}^\dagger\right), \quad [1]$$

where the n_{th} exciton has site energy of ε_n and the exciton is coupled to the cavity mode of energy ω_{c} with a light–matter coupling strength of $\hbar g_{\mathrm{c}}$. Here, $\hat{\sigma}_n^\dagger = |e_n\rangle\langle g_n|$ and $\hat{\sigma}_n = |g_n\rangle\langle e_n|$ create and annihilate an excitation on the n_{th} molecule, respectively, with $|g_n\rangle$ and $|e_n\rangle$ as the ground and excited states for molecule n.

Further, each molecular exciton is coupled to a set of independent phonon bath (with the identical spectral density, see Eq. **21**), described by $\hat{H}_{\mathrm{b}} = \sum_{n=1}^{N}\sum_{\nu} \hbar\omega_\nu(\hat{b}_{n,\nu}^\dagger \hat{b}_{n,\nu} + \frac{1}{2})$, where $\hat{b}_{n,\nu}^\dagger$ and $\hat{b}_{n,\nu}$ are the creation and annihilation operators of the ν_{th} phonon and ω_ν its frequency, with ν labels the phonon DOF. The phonon is coupled to the exciton of the n_{th} molecule, through $\hat{H}_{\mathrm{sb}} = \sum_n \hat{\sigma}_n^\dagger \hat{\sigma}_n \otimes \sum_\nu c_{n,\nu}(\hat{b}_{n,\nu} + \hat{b}_{n,\nu}^\dagger)$, where $c_{n,\nu}$ is the exciton–phonon coupling strength between exciton of the n_{th} molecule and its ν_{th} phonon mode. The molecular dipole operator is expressed as $\hat{\mu} = \sum_{n=1}^{N} \mu_n\left(\hat{\sigma}_n^\dagger + \hat{\sigma}_n\right)$, where μ_n is the magnitude of the transition dipole of excitation for n_{th} molecule, and we have explicitly assumed that the dipole vectors of all molecules are aligned with the cavity field polarization direction. We use the dipole–dipole correlation function of the molecules to compute the multi-time response functions (27–31) (Eq. **8**) and Fourier transform them to obtain 2DES spectra (Eq. **10**). We have not included the static disorder in the exciton energy ε_n (Eq. **1**), because for the CdSe NPL (the physical system we aim to model), the inhomogeneous broadening is negligible (11). The effect of these static disorders on linear lineshape can be found in the previous work (24, 32–35), and our simulation method is general to include them (24).

To interpret the dynamics and spectra, we define the diabatic polariton Hamiltonian as $\hat{H}_{\mathrm{pl}} \equiv \hat{H} - \hat{H}_{\mathrm{sb}} - \hat{H}_b$, with the eigenequation $\hat{H}_{\mathrm{pl}}|\alpha\rangle = \epsilon_\alpha|\alpha\rangle$. For 2DES simulations, we consider both single and double excitation subspaces, with details provided in the Supporting Information. Below, we focus on the single excitation subspace $|j\rangle = \{|\mathrm{G}\rangle \otimes |1\rangle \equiv |\mathrm{G}^1\rangle, |\mathrm{E}_n\rangle \otimes |0\rangle \equiv |\mathrm{E}_n^0\rangle\}$ (where $|\mathrm{G}\rangle \equiv \otimes|g_n\rangle$ and $|\mathrm{E}_n\rangle \equiv |e_n\rangle \otimes |g_m\rangle\ \forall m \neq n$) and introduce polariton states and dark states. We consider degenerate exciton energy $\varepsilon_n = \varepsilon$, and identical light–matter couplings g_{c}, where $\hat{H}_{\mathrm{pl}}$ has a well-known analytic solution, with two bright polariton states (36–40) expressed as follows

$$|+\rangle = \cos\Theta_N\left[\frac{1}{\sqrt{N}}\sum_{n=1}^{N}|\mathrm{E}_n^0\rangle\right] + \sin\Theta_N|\mathrm{G}^1\rangle, \quad [2a]$$

$$|-\rangle = -\sin\Theta_N\left[\frac{1}{\sqrt{N}}\sum_{n=1}^{N}|\mathrm{E}_n^0\rangle\right] + \cos\Theta_N|\mathrm{G}^1\rangle, \quad [2b]$$

where the mixing angle is $\Theta_N = \frac{1}{2}\tan^{-1}[\frac{2\sqrt{N}\hbar g_{\mathrm{c}}}{\Delta}]$ for cavity detuning $\Delta = \hbar\omega_{\mathrm{c}} - \varepsilon$ and $\Theta_N \in [0, \frac{\pi}{2})$. The $N-1$ dark states, indexed with $k \in \{1, \cdots, N-1\}$, are defined as (39, 40)

$$|\mathrm{D}_k\rangle = \frac{1}{\sqrt{N}}\sum_{n=0}^{N-1}\exp\left(2\pi i\frac{nk}{N}\right)|\mathrm{E}_n^0\rangle, \quad [3]$$

where a schematic illustration of UP, LP, and dark states are provided in Fig. 1*E*. The polariton states have the energy of $\varepsilon_\pm = \frac{1}{2}(\varepsilon + \hbar\omega_{\mathrm{c}}) \pm \frac{1}{2}\sqrt{(\varepsilon - \hbar\omega_{\mathrm{c}})^2 + 4N\hbar^2 g_{\mathrm{c}}^2}$, whereas the dark states' energy $\varepsilon_{\mathrm{D}_k} = \varepsilon$ remains the same as the exciton energy. The light–matter detuning is defined as $\Delta_{\mathrm{c}} = \hbar\omega_{\mathrm{c}} - \varepsilon$. The eigenenergies of polariton states are split from the original exciton energy. For the zero-detuning case $\varepsilon = \hbar\omega_{\mathrm{c}}$, the Rabi Splitting is expressed as

$$\hbar\Omega_{\mathrm{R}} = \varepsilon_+ - \varepsilon_- = 2\sqrt{N}\hbar g_{\mathrm{c}}, \quad [4]$$

and the strong coupling limit (26, 39) is achieved when $\Omega_{\mathrm{R}} \gg \frac{1}{2}(\Gamma + \kappa)$, where Γ is the cavity loss rate (linewidth of the cavity transmission spectra, $\tau_{\mathrm{c}} = 1/\Gamma$ is the cavity lifetime) and κ is the exciton linewidth. Detailed discussions related to the polariton population relaxation (39–41) and decoherence (10) can be found in previous work (10, 40). The Hamiltonian in Eq. **1** does not include cavity loss, which corresponds to the far field radiation modes coupling to the cavity mode $\{\hat{a}^\dagger, \hat{a}\}$ (see Appendix E in ref. 42). Here, we treat the cavity loss through Lindblad dynamics (15, 42), with Eq. **20** and a stochastic algorithm detailed in Appendix A of ref. 15. For a cavity loss rate Γ, the quality factor is defined as $Q = \omega_{\mathrm{c}}/\Gamma$.

Polaron Decoupling Effect

Herrera and Spano (7, 8, 43) had shown that strong collective resonant coupling of a cavity field with N emitters can effectively decouple exciton–phonon couplings in a disordered molecular ensemble. This effect originates from the reduction of the vibrational reorganization energy λ when increasing the collective coupling between light and matter, characterized by the Rabi splitting $\Omega_{\mathrm{R}} = 2\sqrt{N}g_{\mathrm{c}}$, where N is the number of molecules and g_{c} is the coupling strength between the cavity mode per molecule. This is because the coupling strength is rescaled by a factor of $1/\sqrt{N}$ for the system–bath coupling terms (39, 40) associated with the polariton states $|+\rangle$ and $|-\rangle$. Below, we briefly discuss how the polaron decoupling effect is quantified within the HTC Hamiltonian framework, and quickly show how it manifests as a reduced effective Huang–Rhys factor and suppressed nuclear displacements. Our previous numerical simulations also demonstrate the narrower linear spectra linewidth as well as associated longer oscillation time in the response functions, demonstrating the polaron decoupling effect (see numerical results provided in *SI Appendix*). Our current work extends the idea of polaron decoupling into 2DES nonlinear spectra, and explicitly demonstrates the prolonged polariton coherence and decoupling from the phonon through the NLS analysis (2).

We express $\hat{H}_{\mathrm{sb}}$ in the polaritonic basis $\hat{H}_{\mathrm{sb}} = \hat{\mathcal{H}}_\pm + \hat{\mathcal{H}}_{\{\pm,\mathrm{D}\}} + \hat{\mathcal{H}}_{\mathrm{D}}$, where $\hat{\mathcal{H}}_\pm$ provides the phonon-mediated transitions between $|+\rangle$ and $|-\rangle$ states, $\hat{\mathcal{H}}_{\{\pm,\mathrm{D}\}}$ provides the phonon-mediated transitions between the $|\pm\rangle$ states to the dark state manifolds $\{|\mathrm{D}_k\rangle\}$, and $\hat{\mathcal{H}}_{\mathrm{D}}$ provides the phonon-mediated transitions among dark states. Under the resonance condition $\hbar\omega_{\mathrm{c}} = \varepsilon$,

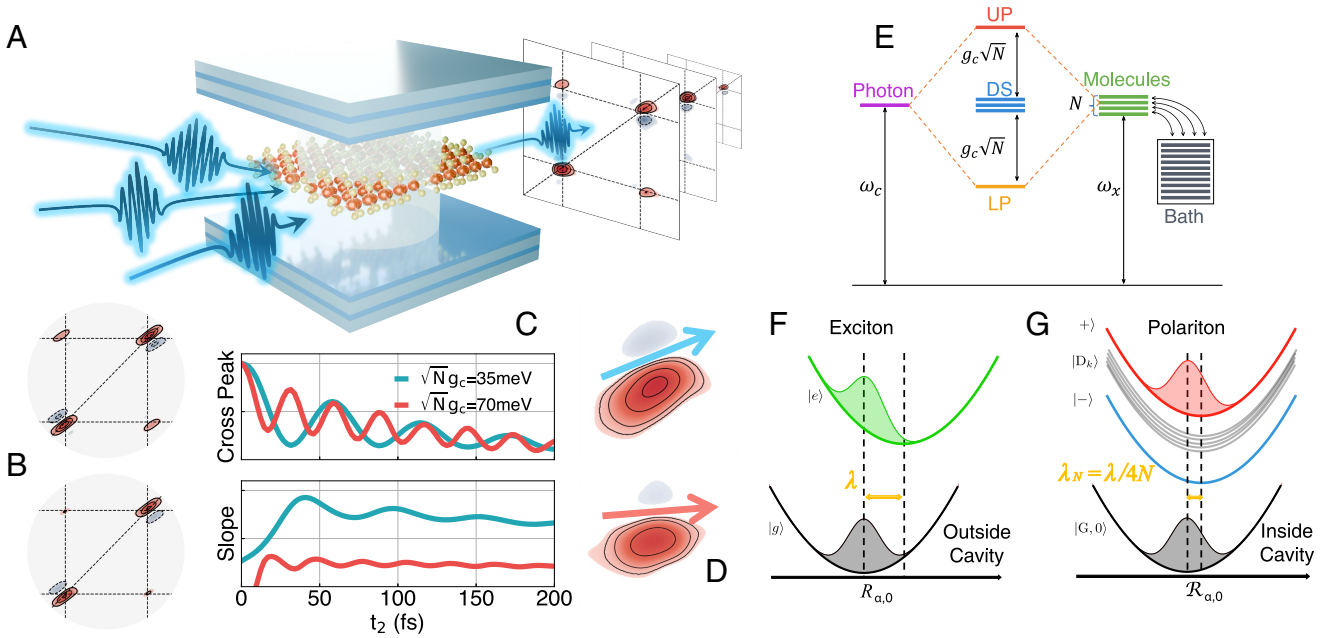

Fig. 1. Schematic illustration of the collective light–matter coupling, the polaron decoupling effect, and its consequences in nonlinear spectra. (*A*) Schematic illustration of a 2DES setup on a polaritonic sample of CdSe NPL coupled to an FP cavity. (*B*) The rephasing 2DES signal at two different t_2 to demonstrate the beating of off-diagonal cross peak. (*C*) The cross-peak and NLS of the lower diagonal peaks at different values of $\sqrt{N}g_c$. (*D*) The lower diagonal 2DES peak (LP diagonal peak) with $\sqrt{N}g_c = 35$ meV and $\sqrt{N}g_c = 70$ meV, and a cavity loss rate of $\Gamma = 10$ meV. (*E*) Schematic illustrations of UP (red), LP (golden), and dark states (DS) through collective exciton–photon hybridization. (*F* and *G*), schematic illustration of the polaron decoupling effect, along the nuclear displacement coordinate.

$\hat{\mathcal{H}}_\pm$ is expressed as follows (10, 39, 40)

$$\hat{\mathcal{H}}_\pm = \frac{1}{2}\Big(|+\rangle\langle+| + |-\rangle\langle-|\Big) \otimes \sum_\nu \frac{c_\nu}{\sqrt{N}}(\hat{b}_{0,\nu} + \hat{b}^\dagger_{0,\nu}) \quad [5]$$
$$- \frac{1}{2}\Big(|+\rangle\langle-| + |-\rangle\langle+|\Big) \otimes \sum_\nu \frac{c_\nu}{\sqrt{N}}(\hat{b}_{0,\nu} + \hat{b}^\dagger_{0,\nu}),$$

where $\hat{b}_{k,\nu} = \frac{1}{\sqrt{N}}\sum_{n=1}^{N} \exp\Big(-2\pi i \frac{nk}{N}\Big)\hat{b}_{n,\nu}$ and $\hat{b}^\dagger_{k,\nu} = \frac{1}{\sqrt{N}}\sum_{n=1}^{N} \exp\Big(-2\pi i \frac{nk}{N}\Big)\hat{b}^\dagger_{n,\nu}$ are the creation and annihilation operators of the ν_{th} bath phonon mode for the k_{th} eigenstates of $\hat{H}_s$. From Eq. **5**, one can see that both $|+\rangle$ state and $|-\rangle$ state are only coupled to the symmetrical phonon modes (with $k = 0$) $\hat{R}_{0,\nu} = (\hat{b}_{0,\nu} + \hat{b}^\dagger_{0,\nu})/\sqrt{2\omega_\nu}$, for both the diagonal term (Holstein coupling) and off-diagonal term (Peierls coupling), with a rescaled coupling strength $c_\nu/\sqrt{N}$. Details of the derivations can be found in ref. 40. Here, ν is the label for the phonon DOF, and ω_ν is the phonon frequency (c.f., Eq. **21**). Note that the displacement between the $|G^0\rangle$ and the $|\pm\rangle$ states is given by Herrera and Spano (8) $\mathcal{R}_{0,\nu} = R_{0,\nu}/2\sqrt{N}$, where $R_{0,\nu} = \sqrt{c_\nu^2/\omega_\nu^3}$ is the displacement between the $|E^0_n\rangle$ and $|G^0\rangle$ states. Thus, the effective reorganization energy $\lambda_N = \frac{1}{2}\sum_\nu \omega_\nu^2 \mathcal{R}^2_{\nu,0}$ between the $|G^0\rangle$ state and the $|\pm\rangle$ states is

$$\lambda_N = \frac{\lambda}{4N}, \quad [6]$$

where $\lambda = \frac{1}{2}\sum_\nu \omega_\nu^2 R^2_{0,\nu}$ is the reorganization energy of the molecular system outside the cavity (c.f., Eq. **22**). A schematic illustration of the polaron decoupling effect is provided in Fig. 1 *F* and *G*. Note that Eq. **6** only accounts for the dynamical disorders (homogeneous broadening) and does not account for static disorder (inhomogeneous broadening), which will likely dominate the exciton contribution of the polariton broadening (44). Under the large N limit, the phonon couplings to the $|\pm\rangle$ are effectively decoupled (8) by $\propto 1/N$. For experiments that couple organic molecules with cavity (45, 46), $N \sim 10^6$ to 10^{12}. For the recent experiments that couple inorganic nanocrystals inside the cavity (e.g., CdSe Nanoplatelets) (11–14), the typical number of emitters is $N \sim 10^3$ to 10^5. As such, the optical lineshape (such as polariton absorption) that corresponds to $|G,0\rangle \rightarrow |\pm\rangle$ optical transition will become much narrower than system outside the cavity (8, 39), and the same effect will also show up in the diagonal peaks of the 2DES spectra (2). Due to the computational cost, we only use a small number of molecules ($N \leq 8$) in the simulations. In our previous work (10), we have found that the population decay dynamics and decoherence are largely controlled by the collective quantity $\sqrt{N}g_c$. As long as N is large enough to ensure a density of states for the dark manifold (24), one can generate nearly identical quantum dynamics by scaling up g_c with a reduced N, as long as $\sqrt{N}g_c$ is kept fixed.

The exciton–phonon coupling term also mediates the transitions between $|\pm\rangle$ and the dark state manifold. Under the resonant condition, these coupling terms are expressed as

$$\hat{\mathcal{H}}_{\{\pm,D\}} = \sum_{k=1}^{N-1} |D_k\rangle\langle+| \otimes \sum_\nu \frac{c_\nu}{\sqrt{2N}}(\hat{b}_{k,\nu} + \hat{b}^\dagger_{-k,\nu}) \quad [7]$$
$$- \sum_{k=1}^{N-1} |D_k\rangle\langle-| \otimes \sum_\nu \frac{c_\nu}{\sqrt{2N}}(\hat{b}_{-k,\nu} + \hat{b}^\dagger_{k,\nu}) + \text{h.c.},$$

These terms facilitate the transition $|+\rangle \rightarrow \{|D_k\rangle\}$, which is responsible for both population decay and the decoherence

of $\rho_{+-}(t)$ (10). Note that for $N = 1$ case, light–matter hybridization will also reduce the effective reorganization energy because both UP and LP are now composed with photon-dressed ground state (15) This effectively reduces the phonon coupling by half (15). It has also been discussed in the context of potential energy hybridization before (26, 47–50). On the other hand, when $N > 1$, the hybrid system contains dark states (Eq. **3**), which serve as one of the main loss channels under the collective coupling regime (10), and the coupling strength per molecule g_c is much weaker than that of the single molecule strong coupling case, even though collectively, $\Omega_R = 2\sqrt{N}g_c$ is large due to the large N.

2DES Spectra

Nonlinear spectroscopy is the ideal tool to provide both direct measurements of coherence lifetime through off-diagonal beatings, as well as the information of vibronic coupling through the NLS that indicate spectral diffusion. Within the linear response limit, the 2D electronic spectra can be obtained by computing the third order response from the four-point correlation function (15, 51)

$$R^{(3)}(t_1, t_2, t_3) = \mathrm{Tr}\left[\hat{\mu}(t_3 + t_2 + t_1)\hat{\mu}^{\times}(t_2 + t_1)\hat{\mu}^{\times}(t_1)\hat{\mu}^{\times}(0)\hat{\rho}^{(g)}\right], \quad [8]$$

where $\hat{\mu}^{\times}\hat{A} \equiv [\hat{\mu}, \hat{A}]$, and $\hat{\rho}^{(g)}$ is the equilibrium ground state density matrix of the system (24). Here, the system is perturbed by external laser pulses at times t_0, t_1, and $t_1 + t_2$, and the system response is detected at $t_1 + t_2 + t_3$. The purely absorptive 2D spectra is computed by adding the rephasing (denoted as $R^{(3)}_{\mathrm{rep}}$) and nonrephasing (denoted as $R^{(3)}_{\mathrm{nrp}}$) contributions expressed as follows

$$R^{(3)}_{\mathrm{rep}}(t_1, t_2, t_3) = R^{(3)}_2 + R^{(3)}_3 + R^{(3)*}_1, \quad [9a]$$

$$R^{(3)}_{\mathrm{nrp}}(t_1, t_2, t_3) = R^{(3)}_1 + R^{(3)}_4 + R^{(3)*}_2. \quad [9b]$$

In Eqs. **9a** and **9b**, the terms on the right-hand side are arranged as individual contributions from (in the order of) stimulated emission (SE), ground state bleach (GSB), and excited state absorption (ESA) signals, respectively. The 2D spectra in the frequency domain are obtained by performing the following Fourier transforms for both rephasing and nonrephasing signals (15, 52),

$$R^{(3)}_{\mathrm{rep}}(\omega_1, t_2, \omega_3) = \int_0^{T_1} dt_1 \int_0^{T_3} dt_3 R^{(3)}_{\mathrm{rep}} e^{i(\omega_3 t_3 - \omega_1 t_1)} S_1 S_3, \quad [10a]$$

$$R^{(3)}_{\mathrm{nrp}}(\omega_1, t_2, \omega_3) = \int_0^{T_1} dt_1 \int_0^{T_3} dt_3 R^{(3)}_{\mathrm{nrp}} e^{i\omega_3 t_3 + i\omega_1 t_1} S_1 S_3, \quad [10b]$$

where $S_i(t_i) = \cos(\pi t_i / 2T_i)$ is a smoothing function for time t_i. The frequency domain pure absorptive 2D spectra are the imaginary part of the total contribution from rephasing (Eq. **10a**) and nonrephasing (Eq. **10b**) signals, expressed as follows

$$R^{(3)}(\omega_1, t_2, \omega_3) = -\Im\mathfrak{m}\left[R^{(3)}_{\mathrm{rep}}(\omega_1, t_2, \omega_3) + R^{(3)}_{\mathrm{nrp}}(\omega_1, t_2, \omega_3)\right]. \quad [11]$$

We use our previously developed lindblad-partially linearized density matrix $\mathcal{L}$-PLDM (15, 24, 25, 51) approach to simulate polariton 2DES spectra. For efficient simulation of 2DES of polaritonic systems with N molecules, we use the recently developed computational algorithm (24, 25) that significantly reduces the numerical cost by taking advantage of the sparsity and the symmetry of the HTC Hamiltonian (24, 25).

Results and Discussion

We present numerical simulations of the polariton 2DES spectra for N-molecules collectively coupled to a single cavity mode. We investigate how collective light–matter interactions influence these nonlinear optical signals, including spectral features that reveal linewidth narrowing, enhanced coherence lifetimes, and signatures of polaron decoupling. Since there are several relevant dynamical time scales in this work, we want to quickly clarify them before moving on to the detailed results. The cavity lifetime (inverse photon rate) is around $\tau_c = \Gamma^{-1} \approx 67$ fs, the characteristic phonon time (inverse of the vibrational frequency) is $\tau_v = \gamma^{-1} \approx 300$ fs (c.f., Eq. **21**), the shortest Rabi oscillation time scale (inverse of the largest Rabi splitting $\Omega_R = 140$ meV considered in this work) is $\tau_\Omega = \Omega_R^{-1} \approx 18$ fs (see Fig. 3*C* the oscillation time), and the longest polariton coherence time we observed from simulation is $\tau \approx 122$ fs under room temperature (Fig. 3*C*), whereas for the same system outside the cavity (or zero coupling limit $g_c \to 0$), the coherence time is $\tau \approx 15$ fs (10). Our previous theoretical development (10) suggests that the coherence time is expressed in Eq. **13**, and the decoherence rate is related to half of the population decay rate from UP (to dark) plus from the cavity photon loss.

2DES Spectra. Fig. 2 shows the simulated pure-absorptive 2DES for $N = 4$ molecules coupled to a single cavity mode, at various population times t_2. The light–matter coupling strength for each molecule is fixed at $\hbar g_c = 200$ cm^{-1} (≈24.8 meV), and the collective coupling produces the lower (LP) and upper polaritons (UP) peaks at $\hbar\omega_- \approx -50$ meV and $\hbar\omega_+ \approx 50$ meV, respectively, with respect to the molecular excitation energy ϵ. This results in a Rabi-Splitting, $\hbar\Omega_R = \hbar\omega_+ - \hbar\omega_- \approx 100$ meV. The cavity loss rate is set to $\Gamma_c = 10$ meV. Each molecule is coupled to a harmonic bath, characterized by a reorganization energy $\hbar\lambda_b = 50$ cm^{-1} (≈6.2 meV) and a characteristic frequency, $\hbar\omega_b = 18$ cm^{-1} (≈2.2 meV). These parameters are consistent with the experimental values for CdSe Nanoplatelets (13) and have been used in previous theoretical polariton spectra simulations (15, 24, 25).

The first column of Fig. 2 shows the rephasing contribution to the pure-absorptive 2DES as a function of the population time t_2. In Fig. 2*A*, two prominent diagonal peaks are observed at (ω_-, ω_-) and (ω_+, ω_+), corresponding to the lower and upper polariton states, respectively. Both peaks exhibit elongations along the diagonal, a hallmark of inhomogeneous broadening due to slow environmental fluctuations caused by low-frequency bath modes. Additionally, negative features appear along the diagonal peaks, due to ESA transitions originating from the polariton states to the doubly excited manifold during the third laser interaction (25). Cross peaks appear at (ω_+, ω_-) and (ω_-, ω_+), which oscillate over t_2, indicating a coherent energy transfer between the upper and lower polariton states (due to the light–matter coupling between $|G^1\rangle$ and $|E^0_n\rangle$) via the $|+\rangle\langle -|$ and $|-\rangle\langle +|$ pathways, respectively.

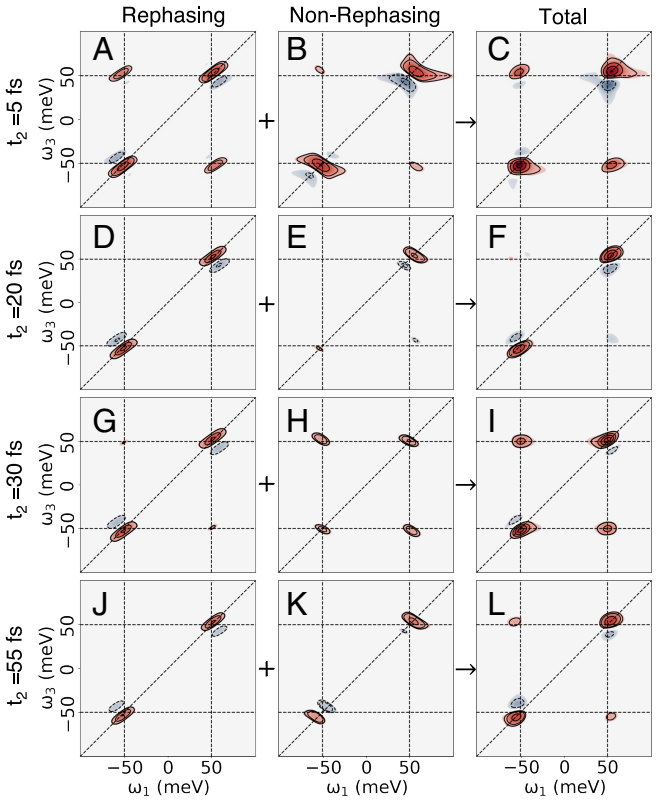

Fig. 2. 2DES signal contributions for $N = 4$ molecules coupled to cavity. Panels (*A–C*), (*D–F*), (*G–I*), and (*J–L*) show the rephasing, non-rephasing, and total pure-absorptive 2DES at population times $t_2 = 5$, 20, 30, and 55 fs, respectively.

Fig. 2*B* shows the nonrephasing contribution of polariton 2DES spectra at $t_2 = 5$ fs. Similar to the rephasing case (in Fig. 2*A*), two diagonal peaks are visible, corresponding to the upper ($|+\rangle\langle+|$) and lower ($|-\rangle\langle-|$) polariton population states. Unlike the rephasing contributions, these diagonal peaks in the nonrephasing signals are elongated along the antidiagonal direction, reflecting homogeneous broadening from fast environmental fluctuations. In this case, the broadening is dominated by contributions from high-frequency intramolecular vibrations and cavity photon loss. Cross-peaks appear at (ω_-, ω_+) and (ω_+, ω_-) are associated with coherence pathways which involve the $|-\rangle\langle+|$ and $|+\rangle\langle-|$ states, respectively. These cross-peaks are noticeably weaker in intensity than those in the rephasing signal, primarily due to the absence of SE pathways in the nonrephasing process and partial cancellation from overlapping ESA contributions (25).

Fig. 2*C* shows the pure-absorptive 2DES signal, obtained by summing the rephasing (panel *A*) and nonrephasing (panel *B*) contributions (Eq. **11**). The diagonal peaks at (ω_-, ω_-) and (ω_+, ω_+) corresponding to the lower $|-\rangle\langle-|$ and upper $|+\rangle\langle+|$ polariton population states, respectively, appear relatively flattened along the excitation axis, ω_1, indicating a partial cancellation of the inhomogeneous broadening exhibited in the rephasing signal by the antidiagonally elongated diagonal signal from the nonrephasing contribution. The cross-peaks, by contrast, remain diagonally elongated, suggesting that coherence-mediated energy transfer between the polariton states is predominantly governed by the rephasing pathways.

Fig. 2 *A*, *D*, *G*, and *J* show the evolution of the rephasing signal at increasing population times t_2. As t_2 progresses, the diagonal peak intensities gradually diminish, reflecting population decay from the polariton states due to cavity loss at a rate of Γ_c. The overall shape remains diagonally elongated due to a persistent inhomogeneous broadening. More notably, the cross-peak intensities exhibit oscillations with a frequency corresponding to the Rabi splitting ($\Omega_R = \omega_+ - \omega_-$), signaling coherent energy exchange between upper and lower polariton states. These oscillations decay over time due to dephasing from both molecular vibrations and cavity loss. The decay of the polariton coherence $|+\rangle\langle-|$ (and $|-\rangle\langle+|$) will be further quantified in Fig. 3.

Fig. 2 *B*, *E*, *H*, and *K* show the nonrephasing contributions at different t_2 delays. Based on the analysis from the Feynman diagrams/Liouville pathways (*SI Appendix*, Fig. S3), SE signals do not give rise to any cross-peaks. Further, the GSB and excited-state absorption (ESA) contributions are expected to completely cancel each other when transition frequencies between the different manifolds are the same. Here, however, we still observe oscillatory cross-peaks that do not fully vanish in the nonrephasing signals. This surviving off-diagonal signal arises from a partial cancellation between ESA and GSB due to a mismatch in transition frequencies between the ground-to-first-excited manifold and the first-to-second-excited manifold (*SI Appendix*, Fig. S2). In contrast to the cross peaks, the diagonal peaks exhibit pronounced oscillations, caused by the presence of $|+\rangle\langle-|$ (and $|-\rangle\langle+|$) coherences during t_2 in the nonrephasing signal. For the diagonal peaks, these coherence pathways are not present in the rephasing pulse sequence (29, 53) and only show up in the nonrephasing pulse sequence. This can be directly verified by inspecting the corresponding Feynman diagrams, where detailed analysis of different peaks and oscillations is provided in *SI Appendix*.

Fig. 2 *C*, *F*, *I*, and *L* present the total pure-absorptive 2DES at various t_2. The cross-peaks exhibit pronounced beating patterns accompanied by evolving lineshapes. Notably, the diagonal peaks, which are initially flattened at $t_2 = 5$ fs (Fig. 2*C*), become diagonally elongated by $t_2 = 20$ fs (Fig. 2*F*). This transient feature arises because the system starts in an uncorrelated tensor product state of the polaritonic ground state and a thermal

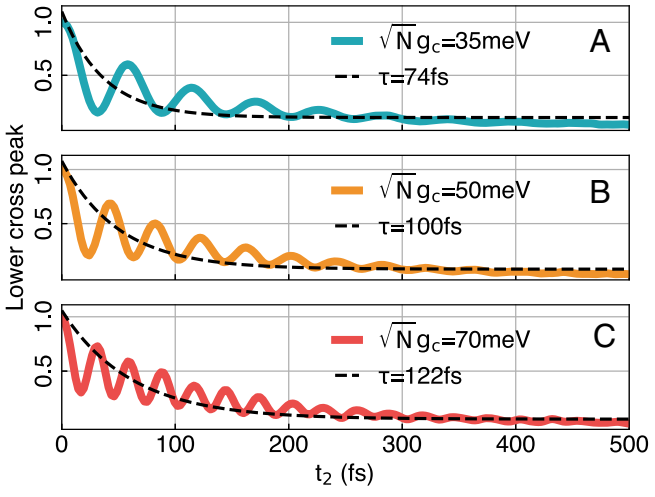

Fig. 3. Lower Cross peak oscillations in 2DES of N-molecules coupled to the cavity. In Panels (*A–C*), the cyan, orange, and red curves represent the cross-peak oscillation for $\sqrt{N}g_c = 35$ meV (with $N = 2$), $\sqrt{N}g_c = 50$ meV (with $N = 4$), and $\sqrt{N}g_c = 70$ meV (with $N = 8$) respectively. The black dotted lines in all the panels represent the lifetime curve fit (using the exponential decay part of Eq. **12**) for the respective curves. The time scale τ should be viewed as the half-lifetime for coherence, based on Eq. **12** The polariton coherence lasts for the time period of 2τ.

distribution of vibrational modes (due to the Franck–Condon excitation), and requires a finite time to build up system–bath correlations (30). Following this initial rise, the system undergoes spectral diffusion (27, 30), causing the diagonal peaks to gradually flatten as seen at $t_2 = 55$ fs. Also, unlike the nonrephasing spectra, we observe that the diagonal peaks do not fluctuate much, indicating that the signal is dominated by rephasing processes.

Coherence Enhancement. The cross-peaks in the pure-absorptive 2DES provide a direct measure of coherent oscillations between upper and lower polariton states. In Fig. 3, we track the time-dependent oscillations of the lower cross-peak from the 2DES for systems where Ω_R increases by raising N while keeping g_c constant. The cyan, orange, and red curves in panels (*A–C*) correspond to the t_2-dependent oscillations of the lower cross-peak intensity for $\hbar\sqrt{N}g_c = 35$ meV, 50 meV, and 70 meV, respectively. As $\Omega_R = 2\sqrt{N}g_c$ increases, the coherence oscillations become faster and persist longer in time, as observed in our previous theoretical studies (10). To extract the coherence lifetime, following the previous theoretical investigation on polariton coherence (10)

$$R^{(3)}(\omega_1, t_2, \omega_3) \propto \mathrm{Re}[\rho_{+-}(t_2)] \sim \frac{1}{2}\cos(\Omega_R \cdot t_2) \cdot e^{-t_2/\tau}, \quad [12]$$

where the $\rho_{+-}(t_2)$ coherence oscillates with the Rabi frequency $\Omega_R \cdot t_2$ and decay exponentially as $e^{-t_2/\tau}$, with τ as the coherence lifetime. This expression was shown to provide an excellent fit to the numerically exact coherence obtained from the quantum dynamics simulations (10). Here, we focus on the $R^{(3)}(\omega_1, t_2, \omega_3)$ signal, with $\omega_1 = 50$ meV and $\omega_3 = -50$ meV, and with the black dashed lines in Fig. 3 showing the exponential decay envelope. We observe that the coherence time τ increases with Ω_R, consistent with prior theoretical results (10). The rising oscillation frequency across panels (*A–C*) reflects the increased Rabi splitting Ω_R with larger N, under a fixed single-molecule coupling strength g_c.

As shown in our previous work (10), the main mechanism of $\rho_{+-}(t) = c_+^*(t) \cdot c_-(t)$ decay in HTC type Hamiltonian is due to the decrease of $c_+^*(t)$ (because of the UP population $\rho_{++}(t) = c_+^*(t) \cdot c_+(t)$ decay to the dark states), while $c_-(t)$ does not have a significant change. The main contribution of the decoherence of $\rho_{+-}(t)$ originates from the population decay from the $|+\rangle$ state to the dark states manifold $\{|D_k\rangle\}$. This population decay is caused by the phonon coupling term $\hat{\mathcal{H}}_{\{\pm,D\}}$ in Eq. **7**. One can thus estimate the coherence time T_2 as follows

$$\frac{1}{\tau} \approx \frac{1}{2}k_{+\to D} + \frac{1}{2}\tau_c^{-1}, \quad [13]$$

where $k_{+\to D}$ is the population decay for the process $|+\rangle \to \{|D_k\rangle\}$, The rate $k_{+\to D}$ can be estimated using Fermi's Golden Rule (FGR) as follows

$$k_{+\to D} = \frac{N-1}{N} \cdot J(\sqrt{N}g_c) \cdot \left[\bar{n}(\sqrt{N}g_c) + 1\right], \quad [14]$$

where $J(\omega)$ is the phonon spectral density expressed in Eq. **21**, and $\bar{n}(\omega) = 1/(e^{\beta\hbar\omega} - 1)$ is the Bose–Einstein distribution function of the phonon. Note that the energy gap between $|+\rangle$ and $|D_k\rangle$ is $\omega_+ - \omega_D = \Omega_R/2 = \sqrt{N}g_c$, which appears in $J(\omega)$ and $\bar{n}(\omega)$ of the FGR expression. For an arbitrary detuning case, there will be an additional factor $[1 + \cos(2\Theta_N)]$ in the FGR expression, see equation S21c in ref. 10. Eqs. **13** and **14** successfully explained the scaling of τ with respect to N and g_c for $\rho_{+-}(t)$. In particular, as increasing the $\Omega_R = 2\sqrt{N}g_c$, the decay rate $k_{+\to D}$ slows down, leading to a longer coherence time for $\rho_{+-}(t)$. Fig. 3 confirms this prediction and indeed suggests a longer coherence time can be achieved by increasing Ω_R. As such, the two main contributors for a longer polariton coherence is 1) reduced effective phonon coupling (due to the partial light nature of polariton) and 2) the phonon bottle neck effect: a larger Rabi splitting Ω_R leads to which a larger energy gap between $|+\rangle$ and $|-\rangle$ states, making phonon-assistant relaxation process less efficient (10). For the early time of the coherence cross peak shown in Fig. 3, as we increase N thus increasing $\sqrt{N}g_c$, the behavior of decoherence changes from a Gaussian-type (see Fig. 3*A* for $t_2 < 20$ fs) to a more Lorentzian-type (see Fig. 3*C*) behavior (10, 39). This type of transition was theoretically explained in ref. 10, due to the transition from the phonon bath dominating regime (which is inhomogeneous) to a cavity loss dominating case (homogeneous).

In this work, we only chose one particular value of λ to model the CdSe NPL (12, 13), and did not perform the scanning of reorganization energy. The effects of prolonged coherence are robust against different values of system–bath couplings (8), because of the delocalization of the polariton and the associated polaron decoupling effect. Quantitatively, if we assume Eqs. **13** and **14**, as well as a Drude–Lorentz model for spectral density in Eq. **21**, then we expect that $k_{+\to D} \propto J_\nu(\sqrt{N}g_c) \propto \lambda\gamma(\sqrt{N}g_c)/(\gamma^2 + Ng_c^2)$. Thus, polariton coherence time $\tau \propto k_{+\to D}^{-1} \propto \sqrt{N}g_c\lambda^{-1}\gamma^{-1}$ (when $\sqrt{N}g_c > \gamma$, which is the case for the current system). Indeed, a larger system–bath coupling means a much shorter coherence to begin with outside the cavity, but the effect of collective light–matter coupling should still prolong the coherence compared to this shorter baseline coherence time, as long as one can increase $\sqrt{N}g_c$ to a larger magnitude to balance the increase of λ. The above discussion might also explain why in organic polariton systems, it is difficult to observe such polariton coherence beating signals in 2DES (2, 17) (in addition to the large static, inhomogeneous disorders) because λ is typically much larger for the organic molecules, with $\lambda \geq 100$ meV, and thus one needs a much larger Ω_R to achieve the same level of polariton coherence enhancement. As a comparison, for CdSe NPL, $\lambda \approx 6.5$ meV (13), and exhibits nearly no inhomogeneous disorders (11).

Our results demonstrate that with a realistic range of reorganization energy for the CdSe Nanoplatelets (11, 13) coupled to the optical cavity, one could generate long-lived coherence at room temperature, up to 200 fs between UP and LP states, when the hybrid system is reaching a collective coupling strength of $\sqrt{N}g_c = 70$ meV (or $\Omega_R = 140$ meV). This range of collective light–matter coupling strength has been realized in our recent experimental setups (11–14).

Several experimental 2DES studies have reported coherent oscillations in UP/LP cross peaks in polaritonic and plexcitonic systems, which were attributed to coherent coupling between the two states (16–18). One of these studies reported a coherence lifetime of 16 fs under a Rabi splitting of 187 meV ($\sqrt{N}g_c = 93.5$ meV) (16), which is significantly shorter compared to the 122 fs dephasing time obtained from our calculations for a comparable magnitude of $\sqrt{N}g_c$. Such differences may arise from variations in cavity architectures and loss parameters, making direct quantitative comparison challenging. Neverthe-

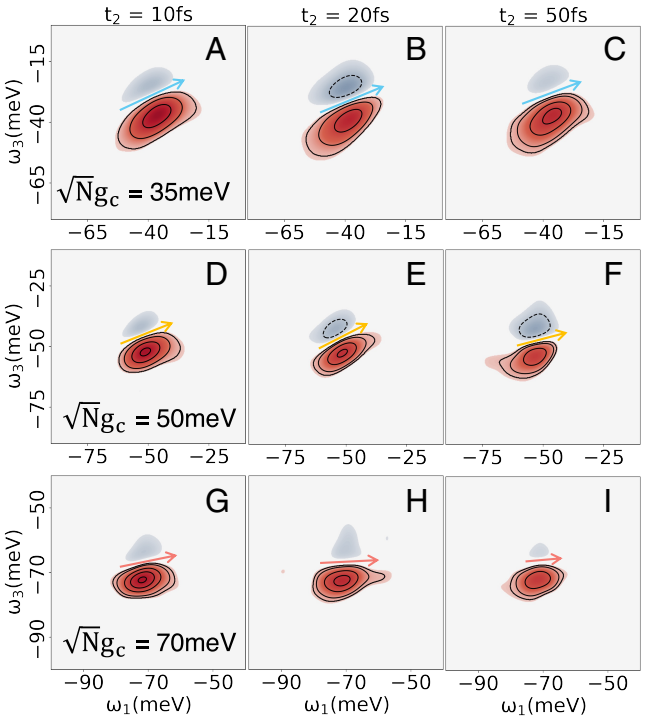

Fig. 4. Lower polariton diagonal peak in the pure-absorptive 2D spectra for various collective coupling strengths. Panels (*A–C*) represent the LP diagonal peak for t_2 = 10 fs, 20 fs, and 50 fs, respectively, for $\sqrt{N}g_c$ = 35 meV. The blue arrow shows the nodal line at each t_2. Panels (*D–F*) represent the LP lineshape for t_2 = 10 fs, 20 fs, and 50 fs, respectively, for $\sqrt{N}g_c$ = 50 meV with the yellow line indicating the nodal line at each t_2. Panels (*G–I*) represent the LP peak at different population times, with the red line representing the nodal line for $\sqrt{N}g_c$ = 70 meV.

less, this discrepancy highlights the need for more systematic experimental characterization of decoherence mechanisms in polaritonic systems to enable meaningful comparison with theoretical predictions. Our proposed setup, using CdSe NPL (very low reorganization energy compared to typical molecular systems) and the FP cavity (which has a much higher quality factor than those plasmonic cavities), should provide the most favorable and ideal case for the direct experimental observations of polariton coherence and verifications of such prolonged coherence under stronger collective light–matter coupling strength.

Polaron Decoupling Effect from 2DES. While the relative widths of diagonal and antidiagonal features in a 2DES provide insight into spectral inhomogeneity, a more direct probe of exciton–phonon coupling strength is given by the NLS of the diagonal peaks (2, 27, 30, 54). In particular, an NLS that tilts toward the excitation axis indicates weaker coupling between the quantum subsystem and the vibrational DOFs, and a reduced system–bath interaction. As such, NLS is a sensitive probe of exciton–phonon coupling by measuring the magnitude of spectral diffusion. Recent 2DES experiments by Watanabe et al. (2) demonstrated that, in the strong coupling regime, increasing the number of molecules per cavity mode volume leads to a flattening of the lower polariton (LP) diagonal peak and associated NLS, as shown in figure 2 of ref. 2.

Fig. 4 shows the time evolution of the LP 2D lineshapes and their corresponding NLSs for systems with $\sqrt{N}g_c$ = 35 meV, 50 meV, and 70 meV (with $N = 2, 4, 8$ accordingly). Panels (*A–C*) display the diagonal LP peak for $\sqrt{N}g_c$ = 35 meV, with the blue arrow indicating the nodal line between the ESA and GSB+SE features. The LP 2DES lineshape maintains a visibly slanted NLS, reaching a peak value of 20° at around t_2 = 50 fs. Panels (*D–F*) are the LP peaks for $\sqrt{N}g_c$ = 50 meV, and the yellow arrow is the nodal line. In this case, the NLS changes from 15° at t_2 = 10 fs to around 10° at t_2 = 50 fs, indicating a faster spectral diffusion and an increased polaron decoupling effect compared to the $\sqrt{N}g_c$ = 35 meV case. For the case of$\sqrt{N}g_c$ = 70 meV, shown in panels (*G–I*), the red NLS line starts nearly flat at 6°, and further reduces to 4°, consistent with strong suppression of system–bath interactions via the polaron decoupling mechanism (2, 8, 39) in the collective regime. Our theoretical results are able to capture the essential experimental features in the previous 2DES studies (see figure 2 in ref. 2).

Fig. 5 presents the NLS between ESA and GSB+SE signals as t_2 varies for different $\sqrt{N}g_c$ values. In panel (*A*), for $\sqrt{N}g_c$ = 35 meV, the cyan curve peaks at ≈19° around t_2 = 40 fs, staying above 10° even at 500 fs, indicating strong exciton–phonon coupling and slow spectral diffusion. In panel (*B*), for $\sqrt{N}g_c$ = 50 meV, the orange curve peaks at 16° at t_2 = 20 fs but drops to ≈7° by 500 fs, suggesting faster spectral diffusion and reduced system–bath interaction. In panel (*C*), for $\sqrt{N}g_c$ = 70 meV, the red curve starts at ≈6° at t_2=10 fs and decreases to 4° at 500 fs. Although the rate of spectral diffusion is slower than in the $\sqrt{N}g_c$ = 50 meV case, the overall polariton–phonon coupling is significantly reduced. For $\sqrt{N}g_c$ = 70 meV , the initial slope is about one-fourth of that for $\sqrt{N}g_c$ = 35 meV and one-third of $\sqrt{N}g_c$ = 50 meV, nearing 0°, indicating near-complete polaron decoupling in the collective limit. Our theoretical results capture the essential features in the 2DES experiments (see figure 3 in ref. 2). With an increasing N, the long-time value of NLS is approaching zero. Here, it is due to the fact that we do not consider the static disorder in the exciton system. When systems exhibit static disorders, the NLS approaches a finite angle at long time as opposed to decaying to zero.

Conclusion

We use state-of-the-art quantum dynamics simulations to investigate polaritonic nonlinear spectroscopy under the collective

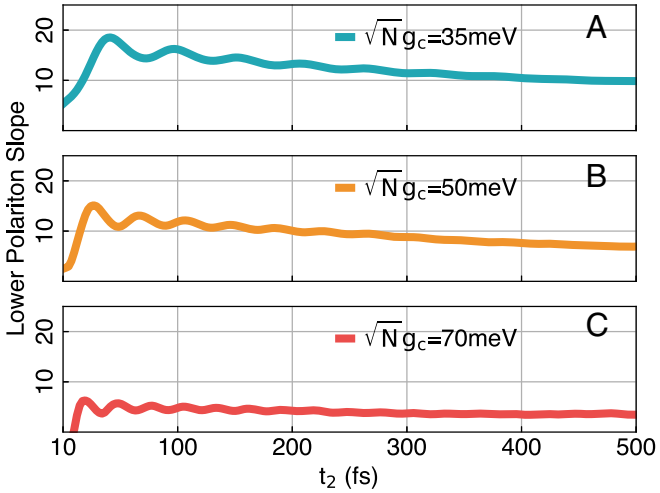

Fig. 5. In Panels (*A–C*), the cyan, orange, and red curves represent the NLS decay as a function of population time t_2 for $\sqrt{N}g_c$ = 35 meV (with $N = 2$), $\sqrt{N}g_c$ = 50 meV (with $N = 4$), and $\sqrt{N}g_c$ = 70 meV (with $N = 8$) respectively.

coupling regime. Our approach is able to capture both non-Markovian bath effects from the molecular environment and the Markovian type of cavity loss (15, 24, 25, 51). We are able to simulate the N-dependent nonperturbative (in system–bath interaction) non-Markovian nonlinear spectra, which are very difficult for other widely used Markovian and perturbative approaches due to the exponential increase of computational cost of the increasing Hilbert space (and consequently the Liouville space) in the second excitation manifold with increasing N.

Our theoretical results reveal that as the collective Rabi splitting $\Omega_R = 2\sqrt{N}g_c$ increases, the polariton linewidths become narrower, which can be seen from the diagonal peaks in 2DES signals. Additionally, as Ω_R increases, both the diagonal peaks and cross-peaks tend to flatten progressively (Fig. 2). Time-resolved analysis of cross-peak oscillations in the pure-absorptive 2DES reveals enhanced coherence times (Fig. 3) as Ω_R increases (when keeping g_c a constant and simply increasing N). This trend reflects the suppression of decoherence pathways via collective coupling (10). The enhancement of coherence is correlated with both the reduction of the effective reorganization energy of the polariton states (2, 7, 8, 39, 40), as well as the phonon bottleneck effect associated with the Rabi splitting, such that when this energy gap is larger than the phonon frequency, single-phonon mediated population relaxation and decoherence are slowed down (10).

We directly characterize the polaron decoupling effect (2, 7, 8) by calculating the NLS between the negative ESA and positive GSB+SE signals in the lower polariton peak of the 2D spectra. The increase in Ω_R flattens the NLS with respect to the excitation axis (Fig. 4), and the slope becomes closer to the full spectral diffusion limit. Our theoretical results agree with the previous experimentally observed by Takahashi and Watanabe (2) using organic molecules coupled to FP cavity. This work demonstrates that with a realistic range of reorganization energy for the CdSe Nanoplatelets (11, 13) coupled to the optical cavity, one could generate long-lived coherence at room temperature, up to 200 fs between UP and LP states, when the hybrid system is reaching a collective coupling strength of $\sqrt{N}g_c = 70$ meV (or $\Omega_R = 140$ meV). This range of collective light–matter coupling strength has been realized in our recent experimental setups (11–14). Future experimental effort will be focused on investigating polariton coherence and polaron decoupling using 2DES (5) for the CdSe NPL system coupled to the cavity (11–14).

Our work provides fundamental insights into the polariton photodynamics in the context of nonlinear spectra, spectral diffusion, coherence, and decoupling from vibrational environment, paving the way for future applications of polaritons in Quantum Information Science.

Materials and Methods

Theory for 2DES Signals. The nonlinear responses in Eq. **8** can be equivalently expressed as (51)

$$R^{(3)}(t_1,t_2,t_3) = -i\mathrm{Tr}\left[\hat{\mu}\mathcal{G}_3\left(\hat{\mu}^{\times}\mathcal{G}_2\left(\hat{\mu}^{\times}\mathcal{G}_1\left(\hat{\mu}_0^{\times}\hat{\rho}^{(g)}\right)\right)\right)\right], \quad \textbf{[15]}$$

where $\mathcal{G}_j\hat{A} = e^{\frac{i}{\hbar}\hat{H}t_j}\hat{A}e^{-\frac{i}{\hbar}\hat{H}t_j}$. These expressions in Eq. **15** can be easily evaluated by using the PLDM approximation (51), where the path-integral expression for the forward and backward propagators is used, and the partial linearization approximation on the nuclear DOF is applied (55, 56). For $R^{(3)}$, the PLDM approximation is expressed as (51)

$$\begin{aligned} R^{(3)}(t_1,t_2,t_3) &\approx -i\sum_{n_3}\sum_{n_2,\tilde{n}_2}\int d\tau_2[\hat{\mu}\tilde{\rho}^{(3)}]_{n_3,n_3}\sum_{n_1,\tilde{n}_1}\int d\tau_1[\hat{\mu}^{\times}\tilde{\rho}^{(2)}]_{n_2,\tilde{n}_2} \\ &\times\sum_{n_0,\tilde{n}_0}\int d\tau_0[\hat{\mu}^{\times}\tilde{\rho}^{(1)}]_{n_1,\tilde{n}_1}[\hat{\mu}\hat{\rho}_g]_{n_0,\tilde{n}_0}\cdot[\hat{\rho}_b]_W, \end{aligned} \quad \textbf{[16]}$$

where $d\tau_j$ are expressed as $d\tau_j \equiv dR_j\cdot dP_j\cdot d\mathbf{c}_j\cdot d\tilde{\mathbf{c}}_j\cdot G_j\cdot\tilde{G}_j$, where R_j and P_j are the "initial" nuclear configuration at time t_j, $\mathbf{c}_j \equiv \{c_a(t_j)\}$ and $\tilde{\mathbf{c}}_j \equiv \{\tilde{c}_a(t_j)\}$ are the complex forward and backward coefficients at time t_j, with $c_a(t_j)$ and $\tilde{c}_a(t_j)$ as the expansion coefficients for the forward and backward mapping trajectories associated with state $|a\rangle$. G_j and $\tilde{G}_j$ are Gaussian distributions (with unit variance and mean = 0) for sampling the forward and backward coefficients (mapping variables). Here, the time t_j (for $t_j \in \{t_1, t_2, t_3\}$) is the time at which the system is perturbed with a laser field. The quantity $\tilde{\rho}^{(j)}$ represents the reduced system density matrix after applying the perturbation at time t_{j-1}, with an initial state of $\tilde{\rho}^{(j-1)} = c_{n_{j-1}}|n_{j-1}\rangle\langle\tilde{n}_{j-1}|\tilde{c}^*_{\tilde{n}_{j-1}}$, and evolved during the time $t \in [t_{j-1}, t_j]$. The evolved density matrix elements can be expressed as

$$\langle n_j|\tilde{\rho}^{(j)}|\tilde{n}_j\rangle = \left(\frac{1}{2}c_{n_j}(t_j)\cdot c^*_{n_{j-1}}\right)\cdot\left(\frac{1}{2}\tilde{c}^*_{\tilde{n}_j}(t_j)\cdot\tilde{c}_{\tilde{n}_{j-1}}\right). \quad \textbf{[17]}$$

Further, $[\hat{\rho}_b]_W$ is the Wigner transform of the bath (phonon)'s initial density operator. Details of this approach can be found in ref. 25.

In Eq. **8**, $R^{(3)}$ can be separated into eight different Liouville pathways, each of which can be categorized as either rephasing or nonrephasing signals. Four of these Liouville pathways correspond to

$$R_1^{(3)} = -i\mathrm{Tr}[\hat{\mu}(t_3+t_2+t_1)\hat{\mu}(0)\hat{\rho}_g\hat{\mu}(t_1)\hat{\mu}(t_1+t_2)], \quad \textbf{[18a]}$$

$$R_2^{(3)} = -i\mathrm{Tr}[\hat{\mu}(t_3+t_2+t_1)\hat{\mu}(t_1)\hat{\rho}_g\hat{\mu}(0)\hat{\mu}(t_2+t_1)], \quad \textbf{[18b]}$$

$$R_3^{(3)} = -i\mathrm{Tr}[\hat{\mu}(t_3+t_2+t_1)\hat{\mu}(t_2+t_1)\hat{\rho}_g\hat{\mu}(0)\hat{\mu}(t_1)], \quad \textbf{[18c]}$$

$$R_4^{(3)} = -i\mathrm{Tr}[\hat{\mu}(t_3+t_2+t_1)\hat{\mu}(t_2+t_1)\hat{\mu}(t_1)\hat{\mu}(0)\hat{\rho}_g], \quad \textbf{[18d]}$$

while the other four pathways can be constructed from the complex conjugate of Eqs. **18a** to **18d**. Similar to Eq. **16**, the individual Liouville pathways in Eq. **18** can also be expressed in the PLDM response function formalism,

Details of Cavity Loss Dynamics. The cavity loss channel from state $|G^1\rangle$ to state $|G^0\rangle$ can be described by the loss operator

$$\hat{L} = |G^0\rangle\langle G^1|. \quad \textbf{[19]}$$

The dissipator $\mathcal{L}_{\hat{L}}$ accounts for the cavity loss channel, causing the system to relax

$$\mathcal{L}_{\hat{L}}[\hat{\rho}_Q] = \Gamma\left(\hat{L}\hat{\rho}_Q\hat{L}^{\dagger} - \frac{1}{2}\{\hat{L}^{\dagger}\hat{L}, \hat{\rho}_Q\}\right), \quad \textbf{[20]}$$

where Γ is the rate of relaxation of the jump operator which quantifies the coupling strength of the system to the environment, and $\{\hat{A}, \hat{B}\} = \hat{A}\hat{B} + \hat{B}\hat{A}$ is the anticommutator, and $\hat{\rho}_Q = \mathrm{Tr}_b[\hat{\rho}]$ is the reduced density matrix operator for the quantum subsystem by tracing out all bath DOF. Eq. **20** was simulated using the stochastic Lindblad approach when combined with the path-integral quantum dynamics approaches, detailed in Appendix A in ref. 15. In this study, Γ is the cavity loss rate, and the cavity quality factor is defined as $\mathcal{Q} = \hbar\omega_c/\Gamma$.

Details of Model Systems. The system–bath interactions are determined by the spectral density (57, 58)

$$J(\omega) = \pi \sum_{\nu} \frac{c_\nu^2}{2\omega_\nu} \delta(\omega - \omega_\nu) = \frac{2\lambda\gamma\omega}{\gamma^2 + \omega^2}, \quad [21]$$

where we use the Drude–Lorentz model, γ is the bath characteristic frequency, and the reorganization energy is

$$\lambda = \frac{1}{\pi} \int_0^\infty d\omega \frac{J(\omega)}{\omega} = \sum_{\nu} \frac{c_\nu^2}{2\omega_\nu^2} = \frac{1}{2} \sum_{\nu} \omega_\nu^2 R_{0,\nu}^2 \quad [22]$$

for all molecules, where $R_{0,\nu} = c_\nu/\omega_\nu^2$ is the displacement between the $|E_n^0\rangle$ and $|G^0\rangle$ states. Here, we use the following parameters: excitation energy $\epsilon = 2.0$ eV, the bath reorganization energy $\lambda = 50\ \text{cm}^{-1}$, and the bath characteristic frequency $\gamma = 18\ \text{cm}^{-1}$, which are the typical parameters for CdSe Nanoplatelets (see schematic illustration in Fig. 1*A*) which has been shown to couple strongly to a dielectric optical cavity (11, 12).

Computational Approaches. We applied recently developed theoretical approaches for the efficient calculations of the polariton 2DES spectra using the $\mathcal{L}$-PLDM approach (15, 24, 25). First, we take advantage of sparsity and the symmetry of the HTC Hamiltonian (24), which allows one to reduce the cost of acting the polariton Hamiltonian onto a state vector to the linear order of the number of states, instead of the quadratic order. Second, we apply the Chebyshev series expansion approach for quantum dynamics propagation (24) and simulate the polariton dynamics in the HTC system, allowing one to use a much larger time step for propagation and only requiring a few recursive operations of the Polariton Hamiltonian acting on state vectors (24). Third, we apply an efficient importance sampling scheme (25) to compute the sums in Eq. **16** in the PLDM-2DES response function, which allows us to significantly reduce the computational costs (15, 25).

Data, Materials, and Software Availability. The source code have been deposited in Github (https://github.com/EliousMondal/PySpec) (59). All other data are included in the manucript and/or *SI Appendix*.

ACKNOWLEDGMENTS. This work was supported by the Department of Energy, Office of Science, Office of Basic Energy Sciences, under Grant No. DE-SC0022171 and DE-SC0026212, the NSF Award under Grant No. CHE-2244683, the Air Force Office of Scientific Research (AFOSR) under the award number FA9550-19-1-0074, the University Research Award from the University of Rochester, as well as the University of Rochester Office of the Vice President for Research, the School of Medicine and Dentistry, and Arts, Sciences & Engineering via the Center for Integrated Research Computing (CIRC) through the CIRC pilot award. The work at Boston University was supported by the U.S. Department of Energy, Office of Science, Office of Basic Energy Sciences under Award No. DE-SC0026384 awarded to M.S. M.E.M. appreciates the support from the Messersmith Fellowship by the Department of Chemistry at the University of Rochester. Computing resources were provided by the CIRC at the University of Rochester. M.E.M. appreciates valuable discussions and comments from Ben Chng.

Author affiliations: [a]Department of Chemistry, University of Rochester, Rochester, NY 14627; [b]Department of Chemistry, Boston University, Boston, MA 02215; [c]Department of Chemistry, Boston University Photonics Center, Boston, MA 02215; [d]The Institute of Optics, Hajim School of Engineering, University of Rochester, Rochester, NY 14627; [e]Department of Physics and Astronomy, University of Rochester, Rochester, NY 14627; [f]Center for Coherence and Quantum Science, University of Rochester, Rochester, NY 14627; and [g]Department of Physics, University of Michigan, Ann Arbor, MI 48109

1. T. W. Ebbesen, Hybrid light-matter states in a molecular and material science perspective. *Acc. Chem. Res.* **49**, 2403–2412 (2016).
2. S. Takahashi, K. Watanabe, Decoupling from a thermal bath via molecular polariton formation. *J. Phys. Chem. Lett.* **11**, 1349–1356 (2020).
3. S. T. Wanasinghe *et al*., Motional narrowing through photonic exchange: Rational suppression of excitonic disorder from molecular cavity polariton formation. *J. Phys. Chem. Lett.* **15**, 2405–2418 (2024).
4. E. O. Odewale, S. T. Wanasinghe, A. S. Rury, Assessing the determinants of cavity polariton relaxation using angle-resolved photoluminescence excitation spectroscopy. *J. Phys. Chem. Lett.* **15**, 5705–5713 (2024).
5. M. Son *et al*., Energy cascades in donor-acceptor exciton-polaritons observed by ultrafast two-dimensional white-light spectroscopy. *Nat. Commun.* **13**, 7305 (2022).
6. S. Dhamija, M. Son, Mapping the dynamics of energy relaxation in exciton-polaritons using ultrafast two-dimensional electronic spectroscopy. *Chem. Phys. Rev.* **5**, 041309 (2024).
7. F. Herrera, F. C. Spano, Cavity-controlled chemistry in molecular ensembles. *Phys. Rev. Lett.* **116**, 238301 (2016).
8. F. Herrera, F. C. Spano, Theory of nanoscale organic cavities: The essential role of vibration-photon dressed states. *ACS Photon.* **5**, 65–79 (2018).
9. R. M. Gracia, G. J. Russo, S. Park, L. Kinziabulatova, M. Son, Modulation of vibronic transitions in chlorophyll a through strong light-matter coupling. *J. Mater. Chem. C* **13**, 21367–21374 (2025).
10. B. X. Chng *et al*., Mechanism of molecular polariton decoherence in the collective light-matter couplings regime. *J. Phys. Chem. Lett.* **15**, 11773–11783 (2024).
11. L. Qiu *et al*., Molecular polaritons generated from strong coupling between CdSe nanoplatelets and a dielectric optical cavity. *J. Phys. Chem. Lett.* **12**, 5030–5038 (2021).
12. O. Morshed *et al*., Room-temperature strong coupling between CdSe nanoplatelets and a metal-DBR Fabry–Pérot cavity. *J. Chem. Phys.* **161**, 014710 (2024).
13. M. Amin *et al*., Cavity controlled upconversion in CdSe nanoplatelet polaritons. *ACS Nano* **18**, 21388–21398 (2024).
14. F. Freire-Fernández *et al*., Room-temperature polariton lasing from CdSe core-only nanoplatelets. *ACS Nano* **18**, 15177–15184 (2024).
15. M. E. Mondal *et al*., Quantum dynamics simulations of the 2D spectroscopy for exciton polaritons. *J. Chem. Phys.* **159**, 094102 (2023).
16. N. Peruffo, F. Mancin, E. Collini, Coherent dynamics in solutions of colloidal plexcitonic nanohybrids at room temperature. *Adv. Opt. Mater.* **11**, 2203010 (2023).
17. D. Timmer *et al*., Plasmon mediated coherent population oscillations in molecular aggregates. *Nat. Commun.* **14**, 8035 (2023).
18. M. Russo *et al*., Direct evidence of ultrafast energy delocalization between optically hybridized J-aggregates in a strongly coupled microcavity. *Adv. Opt. Mater.* **12**, 2400821 (2024).
19. D. Timmer *et al*., Ultrafast transition from coherent to incoherent polariton nonlinearities in a hybrid 1L-WS_2/plasmon structure. *Nat. Nanotechnol.* **21**, 216–222 (2026).
20. H. Li *et al*., The optical signatures of stochastic processes in many-body exciton scattering. *Annu. Rev. Phys. Chem.* **74**, 467–492 (2023).
21. D. Gallego-Valencia, L. Mewes, J. Feist, J. L. Sanz-Vicario, Coherent multidimensional spectroscopy in polariton systems. *Phys. Rev. A* **109**, 063704 (2024).
22. Z. Zhang, X. Nie, D. Lei, S. Mukamel, Multidimensional coherent spectroscopy of molecular polaritons: Langevin approach. *Phys. Rev. Lett.* **130**, 103001 (2023).
23. D. Finkelstein-Shapiro, P. A. Mante, S. Balci, D. Zigmantas, T. Pullerits, Non-Hermitian Hamiltonians for linear and nonlinear optical response: A model for plexcitons. *J. Chem. Phys.* **158**, 104104 (2023).
24. M. E. Mondal, A. N. Vamivakas, S. T. Cundiff, T. D. Krauss, P. Huo, Polariton spectra under the collective coupling regime. I. Efficient simulation of linear spectra and quantum dynamics. *J. Chem. Phys.* **162**, 014114 (2025).
25. M. E. Mondal, A. N. Vamivakas, S. T. Cundiff, T. D. Krauss, P. Huo, Polariton spectra under the collective coupling regime. II. 2D non-linear spectra. *J. Chem. Phys.* **162**, 074110 (2025).
26. A. Mandal *et al*., Theoretical advances in polariton chemistry and molecular cavity quantum electrodynamics. *Chem. Rev.* **123**, 9786–9879 (2023).
27. L. Valkunas, D. Abramavicius, T. Mancal, *Molecular Excitation Dynamics and Relaxation: Quantum Theory and Spectroscopy* (John Wiley & Sons, 2013).
28. E. Collini, 2D electronic spectroscopic techniques for quantum technology applications. *J. Phys. Chem. C* **125**, 13096–13108 (2021).
29. A. M. Brańczyk, D. B. Turner, G. D. Scholes, Crossing disciplines–A view on two-dimensional optical spectroscopy. *Ann. Phys.* **526**, 31–49 (2014).
30. P. Hamm, M. Zanni, *Concepts and Methods of 2D Infrared Spectroscopy* (Cambridge University Press, 2011).
31. A. Gelzinis, R. Augulis, V. Butkus, B. Robert, L. Valkunas, Two-dimensional spectroscopy for non-specialists. *Biochim. Biophys. Acta, Bioenerg.* **1860**, 271–285 (2019).
32. B. M. Weight, S. Tretiak, Y. Zhang, Diffusion quantum Monte Carlo approach to the polaritonic ground state. *Phys. Rev. A* **109**, 032804 (2024).
33. J. Yuen-Zhou, A. Koner, Linear response of molecular polaritons. *J. Chem. Phys.* **160**, 154107 (2024).
34. K. Schwennicke, N. C. Giebink, J. Yuen-Zhou, Extracting accurate light-matter couplings from disordered polaritons. *Nanophotonics* **13**, 2469–2478 (2024).
35. Z. Zhou, H. T. Chen, J. E. Subotnik, A. Nitzan, Interplay between disorder, local relaxation, and collective behavior for an ensemble of emitters outside versus inside a cavity. *Phys. Rev. A* **108**, 023708 (2023).
36. J. A. Campos-Gonzalez-Angulo, R. F. Ribeiro, J. Yuen-Zhou, Generalization of the Tavis-Cummings model for multi-level anharmonic systems. *New J. Phys.* **23**, 063081 (2021).
37. C. A. DelPo *et al*., Polariton transitions in femtosecond transient absorption studies of ultrastrong light-molecule coupling. *J. Phys. Chem. Lett.* **11**, 2667–2674 (2020).
38. J. A. Campos-Gonzalez-Angulo, J. Yuen-Zhou, Generalization of the Tavis-Cummings model for multi-level anharmonic systems: Insights on the second excitation manifold. *J. Chem. Phys.* **156**, 063081 (2022).
39. W. Ying, M. E. Mondal, P. Huo, Theory and quantum dynamics simulations of exciton-polariton motional narrowing. *J. Chem. Phys.* **161**, 064105 (2024).
40. Y. Lai, W. Ying, P. Huo, Non-equilibrium rate theory for polariton relaxation dynamics. *J. Chem. Phys.* **161**, 104109 (2024).
41. D. Hu, B. X. Chng, W. Ying, P. Huo, Trajectory-based non-adiabatic simulations of the polariton relaxation dynamics. *J. Chem. Phys.* **162**, 124113 (2025).

42. E. R. Koessler, A. Mandal, P. Huo, Incorporating Lindblad decay dynamics into mixed quantum-classical simulations. *J. Chem. Phys.* **157**, 064101 (2022).
43. F. Herrera, F. C. Spano, Absorption and photoluminescence in organic cavity QED. *Phys. Rev. A: At. Mol. Opt. Phys.* **95**, 053867 (2017).
44. R. Houdré, R. P. Stanley, M. Ilegems, Vacuum-field Rabi splitting in the presence of inhomogeneous broadening: Resolution of a homogeneous linewidth in an inhomogeneously broadened system. *Phys. Rev. A* **53**, 2711–2715 (1996).
45. J. del Pino, J. Feist, F. J. Garcia-Vidal, Quantum theory of collective strong coupling of molecular vibrations with a microcavity mode. *New J. Phys.* **17**, 053040 (2015).
46. J. A. Campos-Gonzalez-Angulo, R. F. Ribeiro, J. Yuen-Zhou, Resonant catalysis of thermally activated chemical reactions with vibrational polaritons. *Nat. Commun.* **10**, 4685 (2019).
47. J. Galego, F. J. Garcia-Vidal, J. Feist, Cavity-induced modifications of molecular structure in the strong-coupling regime. *Phys. Rev. X* **5**, 041022 (2015).
48. R. F. Ribeiro, L. A. Martínez-Martínez, M. Du, J. Campos-Gonzalez-Angulo, J. Yuen-Zhou, Polariton chemistry: Controlling molecular dynamics with optical cavities. *Chem. Sci.* **9**, 6325–6339 (2018).
49. A. Mandal, P. Huo, Investigating new reactivities enabled by polariton photochemistry. *J. Phys. Chem. Lett.* **10**, 5519–5529 (2019).
50. A. Mandal, T. D. Krauss, P. Huo, Polariton-mediated electron transfer via cavity quantum electrodynamics. *J. Phys. Chem. B* **124**, 6321–6340 (2020).
51. J. Provazza, F. Segatta, M. Garavelli, D. F. Coker, Semiclassical path integral calculation of nonlinear optical spectroscopy. *J. Chem. Theory Comput.* **14**, 856–866 (2018).
52. J. R. Mannouch, J. O. Richardson, A partially linearized spin-mapping approach for simulating nonlinear optical spectra. *J. Chem. Phys.* **156**, 024108 (2022).
53. P. H. Lambrev, P. Akhtar, H. S. Tan, Insights into the mechanisms and dynamics of energy transfer in plant light-harvesting complexes from two-dimensional electronic spectroscopy. *Biochim. Biophys. Acta, Bioenerg.* **1861**, 148050 (2020).
54. K. Kwak, S. Park, I. J. Finkelstein, M. D. Fayer, Frequency-frequency correlation functions and apodization in two-dimensional infrared vibrational echo spectroscopy: A new approach. *J. Chem. Phys.* **127**, 124503 (2007).
55. P. Huo, I. Miller, F. Thomas, D. F. Coker, Communication: Predictive partial linearized path integral simulation of condensed phase electron transfer dynamics. *J. Chem. Phys.* **139**, 151103 (2013).
56. M. Lee, P. Huo, D. Coker, Semi-classical path integral dynamics: Photosynthetic energy transfer with realistic environment interactions. *Ann. Rev. Phys. Chem.* **67**, 639 (2016).
57. A. O. Caldeira, A. J. Leggett, Path integral approach to quantum Brownian motion. *Physica A* **121**, 587–616 (1983).
58. A. Nitzan, *Chemical Dynamics in Condensed Phases: Relaxation, Transfer, and Reactions in Condensed Molecular Systems* (Oxford University Press, 2024).
59. E. Mondal, EliousMondal/PySpec. GitHub. https://github.com/EliousMondal/PySpec. Deposited 23 July 2025.